J Adv Ceram

Research Article

Enhanced humidity-sensing performance of (Zr^{4+}/Sb^{5+})-codoped TiO_2 ceramics with giant dielectric properties

Noppakorn Thanamoon[1,2], Nateeporn Thongyong[1,3], Kaniknun Sreejivungsa[4], Narong Chanlek[3], Prasit Thongbai[1,2,✉]

Cite this article: Thanamoon N, Thongyong N, Sreejivungsa K, et al. *J Adv Ceram* 2025, **14**(1): 9221005. https://doi.org/10.26599/JAC.2024.9221005

ABSTRACT: In this study, $(Zr_{0.5}/Sb_{0.5})_xTi_{1-x}O_2$ ceramics with x = 0.01, 0.025, and 0.05 were prepared via the solid-state reaction (SSR) method. A pure phase of rutile TiO_2 with a highly dense microstructure and relative density (ρ_r) higher than 96% was detected in all the sintered ceramics. The mean grain size was reduced, but the dielectric permittivity (ε') increased. The giant dielectric properties were tested to investigate their possible use in capacitors and capacitive humidity sensors under various relative humidity (RH) levels ranging from 30% to 95% RH. $(Zr_{0.5}/Sb_{0.5})_xTi_{1-x}O_2$ ceramics present a giant ε' of ~$(4.82–7.39)\times10^4$ and a low loss tangent ($\tan\delta \approx 0.031–0.106$ at 1 kHz), indicating attractive giant dielectric properties. This observation was attributed to both intrinsic and extrinsic effects. For the humidity sensing properties, the best humidity sensing properties were observed in the ceramics with x = 0.05, with a sensitivity of ~237%pF/%RH, a low hysteresis error (~1.6%), and fast response/recovery time of ~12 s/16 s at 1 kHz. The point defects of $Sb_{Ti}^{\cdot}$ and $V_O^{\cdot\cdot}$ were claimed to be active centers for water absorption. Furthermore, impedance spectroscopy (IS) analysis revealed that changes in the dielectric properties with varying RH levels were also influenced by interfacial polarization at the surface layer and grain boundaries.

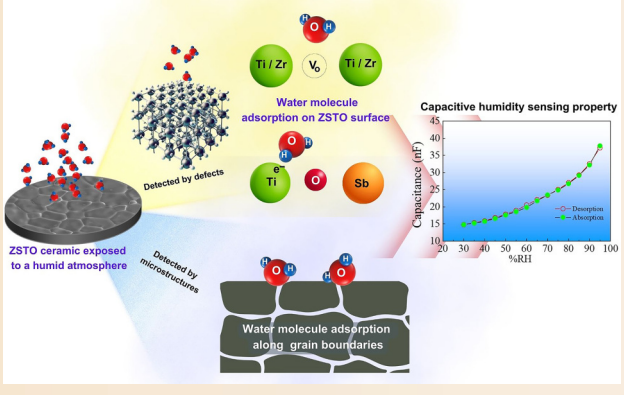

KEYWORDS: humidity sensor; humidity-sensing properties; giant/colossal dielectric permittivity; X-ray photoelectron spectroscopy (XPS); point defect; TiO_2

1 Introduction

The demand for advanced humidity-sensing materials has increased across sectors such as environmental monitoring, healthcare, and industrial applications due to the rapid development of human activities [1,2]. Ceramic materials have been widely utilized in both industry and research laboratories as humidity sensor materials owing to their mechanical strength, chemical stability, and thermophysical stability, which provide distinct advantages [3,4]. Typically, classified as capacitive/impedance or resistive-type, ceramic humidity sensors exhibit changes in their capacitive/impedance or resistive properties in response to fluctuations in humidity levels, making them excellent candidates for humidity sensing applications [5–8].

Over the past decade, considerable research has focused on aliovalent/pentavalent (A^+, A^{2+}, A^{3+}/Nb^{5+}, and Ta^{5+}) [9–14] and isovalent/pentavalent (A^{4+}/Nb^{5+} and Ta^{5+}) [15–17] ions codoped with TiO_2 ceramics, with the aim of developing giant dielectric materials characterized by high dielectric permittivity ($\varepsilon' > 10^4$), which is determined by their capacitive/dielectric properties. The origins of these dielectric properties have been debated, with some attributing them to intrinsic factors such as complex defects-dipoles [9,10,12,13], whereas others propose extrinsic effects such as grain/grain boundary microstructures [14,15,18] and surface layer or electrode effects [19–21]. On the basis of these effects, polar water molecules can interact with defect-dipoles on the ceramic surface, along grain boundaries, and within the pore structure of the ceramics. This interaction suggests their potential as humidity-sensing materials. High-permittivity dielectric materials have demonstrated interesting responses to humidity (water in air), similar to $ACu_3Ti_4O_{12}$ (ACTO)-based materials

[1] Giant Dielectric and Computational Design Research Group (GD-CDR), Department of Physics, Faculty of Science, Khon Kaen University, Khon Kaen 40002, Thailand. [2] Institute of Nanomaterials Research and Innovation for Energy (IN-RIE), Faculty of Science, Khon Kaen University, Khon Kaen 40002, Thailand. [3] Synchrotron Light Research Institute (Public Organization), Nakhon Ratchasima 30000, Thailand. [4] Department of Fundamental Science, Faculty of Science and Technology, Surindra Rajabhat University, Surin 32000, Thailand.

✉ Corresponding author. E-mail: pthongbai@kku.ac.th

Received: June 4, 2024; Revised: September 29, 2024; Accepted: November 20, 2024

where A is a divalent cation such as Ca^{2+} or mixed-valent ions with an average oxidation state of +2 [5,8,22,23], CuO [24], and nanocrystalline $Na_{0.5}K_{0.5}NbO_3$ (NKN)-based ceramics [25,26]. In NKN, numerous surface defects and the hygroscopic nature of K^+ and Na^+ ions facilitate easy water adsorption on nanocrystalline particles. In ACTO-based materials, in addition to surface water adsorption, water can be absorbed along grain boundaries near the surface, enhancing the internal barrier layer capacitor (IBLC) effect and consequently increasing ε' and capacitance (C_p) values. However, studies examining the humidity-sensing behavior of codoped TiO_2 ceramics are lacking.

Recently, the capacitive humidity-sensing behavior of tetravalent/pentavalent ion co-doped TiO_2 ceramics, such as (In^{3+}/Nb^{5+})-codoped TiO_2 (INTO) ceramics, has been demonstrated, with a high humidity sensitivity of 229.22 pF/% relative humidity (RH) at 100 Hz [27]. Additionally, (Na^+/Nb^{5+})- and (In_2O_3:SnO_2/Ta^{5+})-codoped TiO_2 (NNTO and ISTTO) ceramics exhibit interesting humidity-sensing properties [28, 29]. It has been suggested that the humidity response of these TiO_2-based materials is influenced by the presence of oxygen vacancies ($V_O^{\cdot\cdot}$) and point defects where Nb^{5+} or Ta^{5+} substitutes for Ti^{4+} ($Nb_{Ti}^{\cdot}$/$Ta_{Ti}^{\cdot}$) [27–29]. These defects, induced by dopant substitution at the ceramic surface, result in changes in the dielectric properties due to surface layer effects. Furthermore, isovalent/pentavalent codoping in TiO_2, such as (Zr^{4+}/Nb^{5+}) and (Zr^{4+}/Ta^{5+}), can lead to the formation of point defects such as $Nb_{Ti}^{\cdot}$ and $Ta_{Ti}^{\cdot}$ [16,17]. $V_O^{\cdot\cdot}$ has also been detected in these materials, likely because of oxygen loss at high sintering temperatures [17]. Humidity sensors based on NNTO powder deposited on Au interdigitated electrodes were also fabricated and showed promising performance [29]. However, the maximum hysteresis error (γ_H) remained high at 10.5%, whereas the γ_H values for NNTO, INTO, and ISTTO bulk ceramics were reported to be 4.2% [30], 7.3% [27], and 3.6% [28], respectively. These findings indicate that further improvements in reducing hysteresis are necessary for practical applications.

In the case of undoped $ACu_3Ti_4O_{12}$-based materials, the humidity response is attributed to water molecule adsorption, which affects the potential barrier capacitance at the $ACu_3Ti_4O_{12}$/electrode interface and at the grain boundaries, ultimately influencing the total C_p of $ACu_3Ti_4O_{12}$ [5,8,22,23]. In our previous works [31–33], we reported that the IBLC effect in multidoped TiO_2 and $ACu_3Ti_4O_{12}$ can be enhanced by doping with an isovalent Sn^{4+} dopant. Therefore, both defect-induced polarization and interfacial polarization likely contribute to the interaction of the materials with water molecules, motivating further studies on the humidity-sensing behavior of isovalent/pentavalent ion-doped TiO_2 ceramics. The giant dielectric properties of these ceramics are expected to arise from induced defects and extrinsic effects. Moreover, the introduction of high-electronegativity dopants could enhance the attraction of water molecules. Compared with pentavalent Nb^{5+} and Ta^{5+} ions, the Sb^{5+} ion is more electronegative, making it a promising candidate for enhancing the humidity sensing performance.

On the basis of the literature, this study investigated the capacitive humidity sensing properties of TiO_2 doped with isovalent Zr^{4+} ions and pentavalent Sb^{5+} ions, forming $(Zr_{0.5}/Sb_{0.5})_xTi_{1-x}O_2$ (ZSTO), where x = 0.01, 0.025, and 0.05, referred to as 1% ZSTO, 2.5% ZSTO, and 5% ZSTO, respectively. The ZSTO ceramics were prepared via the solid-state reaction (SSR) method and sintered at 1450 °C for 4 h. The sintered ZSTO ceramics exhibited a giant ε' ranging from ~4.8×10^4 to ~7.4×10^4. Notably, the 5% ZSTO ceramics demonstrated optimal humidity sensing properties, with a humidity sensitivity of ~237 pF/%RH at 1 kHz, a low γ_H of ~1.6%, and fast response and recovery time (t_{Res}/t_{Rec} ≈ 12 s/16 s). This study suggests that ZSTO ceramics have significant potential for use in humidity sensors. Further investigations into the origin of the humidity behavior in ZSTO ceramics will be discussed in detail.

2 Experimental

ZrO_2 (99.95% purity, Nanostructured & Amorphous Materials, USA), Sb_2O_5 (99.998% purity, Alfa Aesar, USA), and TiO_2 (99.9% purity, Sigma-Aldrich, USA) powder was used as raw materials to synthesize ZSTO powder. The variable x was set at 0.01, 0.025, and 0.05, corresponding to 1% ZSTO, 2.5% ZSTO, and 5% ZSTO, respectively. The ZSTO powder was prepared via the SSR method. The starting raw materials were mixed via a ball-milling method in ethanol for 24 h. The mixed powder was then dried at 80 °C for 24 h in an oven (UN55, Memmert, Germany). The dried ZSTO powder with different codoping concentrations was subsequently uniaxially pressed into disks with a diameter of 9.5 mm and a thickness of approximately 1.0 mm. The pellets were then sintered at 1450 °C for 4 h at a heating rate of 2 °C/min to obtain the ZSTO ceramics.

To investigate the crystallography of the materials, X-ray diffraction (XRD) analysis was performed via an X-ray diffractometer (EMPYREAN, PANalytical, China). A scanning electron microscope (SEM; Helios nanoLab G3 CX, ThermoFischer (formerly FEI), The Czech Republic) was employed to examine the microstructure and surface morphology. The density of the sintered samples was determined via the Archimedes principle and subsequently calculated as the relative density (ρ_r). The oxidation state of the ceramic samples was analyzed via an X-ray photoelectron spectroscope (XPS; PHI5000 VersaProbe II, SUT-NANOTEC-SLRI Joint Research Facility within the Synchrotron Light Research Institute (SLRI), Thailand). Additionally, a dispersive Raman microscope (Senterra II, Bruker, China) was conducted to investigate the Raman shift of the ceramics.

Before the dielectric properties were measured, the ceramic samples were polished to remove the insulating surface layer, reducing each side by 0.1 mm. The sintered samples had a diameter of 7.8 mm. The electrode configuration consisted of two parallel plates: The bottom electrode was fully coated with Ag, while the top electrode was coated with Ag in a 5.0 mm diameter area. Afterward, the dielectric properties were measured at 25 °C over a frequency range of 40–10^6 Hz via an impedance analyzer (E4990A, KEYSIGHT, USA) with root mean square voltage (V_{rms}) of 500 mV. The humidity-sensing properties were evaluated by measuring the dielectric response of the ceramics across a RH range of 30%–95% RH in an environmental chamber (SH-222, ESPEC, Japan).

3 Results and discussion

Figure 1 presents the XRD analysis of the ZSTO ceramics. The analysis reveals peaks corresponding to the rutile phase of TiO_2, which is consistent with the $P4_2/mnm$ space group per JCPDS file No. 21-1276, indicating a tetragonal crystalline structure in all ceramics [9,18,34]. Notably, no impurity phases were detected, highlighting the high purity of the synthesized ZSTO ceramics. The Rietveld refinement analysis provided further insights into the structural characteristics, as shown in Fig. S1 in the Electronic Supplementary Material (ESM). The obtained structural and fitting parameters are presented in Table S1 in the ESM. As listed

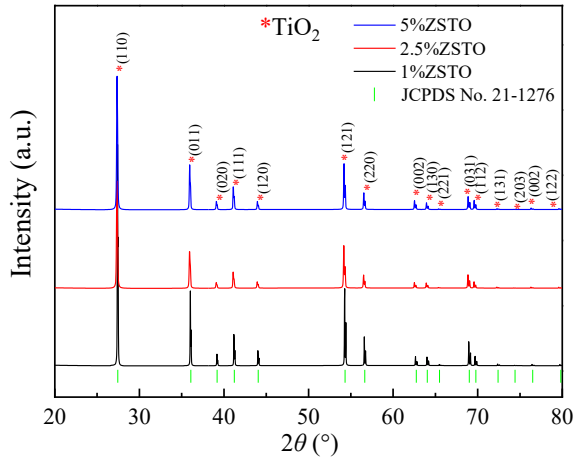

Fig. 1 XRD patterns of ZSTO ceramics compared with standard data for TiO_2.

in Table 1, the analysis revealed that the lattice parameters, *a* and *c*, for the ZSTO ceramics were greater than those of the rutile phase of TiO_2. This suggests structural modifications due to the incorporation of Zr^{4+} and Sb^{5+} ions, as the codopants have larger average ionic radii, Zr^{4+} (r_6 = 72.0 pm) and Sb^{5+} (r_6 = 60.0 pm), compared to the host Ti^{4+} ion (r_6 = 60.5 pm) [35]. Additionally, the increasing lattice parameter ratio (*c*/*a*) with increasing dopant concentration, similar to that of the INTO ceramics [9], suggests that the dopants significantly influence the structural properties of the ZSTO ceramics, potentially leading to lattice expansion or distortion.

The microstructure and morphology of the ZSTO ceramics were examined via SEM, as shown in Fig. 2. The SEM images show dense microstructures, indicating well-compacted ceramic structures. The ρ_r values were calculated to be 97.2%, 97.2%, and 96.5% for the 1%ZSTO, 2.5%ZSTO, and 5%ZSTO ceramics, respectively, indicating effective densification during the sintering process. The mean grain sizes were 20.6±7.0, 17.6±6.8, and 13.9±5.8 μm for the 1%ZSTO, 2.5%ZSTO, and 5%ZSTO samples, respectively. In the inset of Figs. 2(a)–2(c), the grain size distribution histograms closely follow Gaussian curves, indicating a uniform distribution of grain sizes. The observed trend of decreasing grain size with increasing dopant concentration can be attributed to the pinning effect of the Zr and Sb dopants, which hinders grain boundary mobility, resulting in finer grain sizes [36]. The substitution of pentavalent dopants (+5 ions) into Ti^{4+} sites, as observed in Ga^{3+}/Ta^{5+}-codoped TiO_2 [37] and Al^{3+}/Ta^{5+}-codoped $CaCu_3Ti_4O_{12}$ [38], can also reduce the mean grain size due to the

Table 1 Dielectric properties at 1 kHz and 25 °C, lattice constants (*a* and *c*), ratio of lattice constants (*c*/*a*), ρ_r, and mean grain size of ZSTO ceramics

Sample	Dielectric property@1 kHz and 25 °C		Lattice constant (Å)		*c*/*a*	ρ_r (%)	Mean grain size (μm)
	ε'	tanδ	*a*	*c*			
TiO_2 (JCPDS# 21-1276)	—	—	4.593(0)	2.959(0)	0.6442(0)	—	—
1%ZSTO	48,285	0.106	4.594(6)	2.962(6)	0.64482	97.2	20.6±7.0
2.5%ZSTO	72,323	0.046	4.595(8)	2.965(1)	0.64518	97.2	17.6±6.8
5%ZSTO	73,964	0.031	4.594(9)	2.964(9)	0.64526	96.5	13.9±5.8

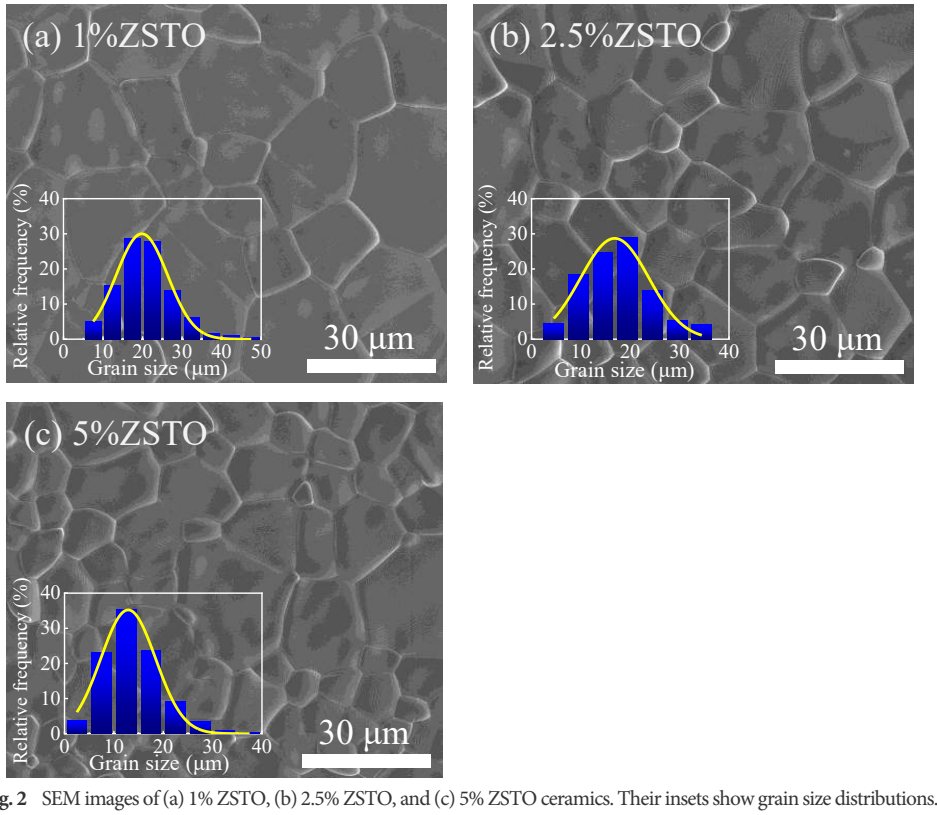

Fig. 2 SEM images of (a) 1% ZSTO, (b) 2.5% ZSTO, and (c) 5% ZSTO ceramics. Their insets show grain size distributions.

清華大学出版社 Tsinghua University Press | SciOpen

space charge effect. As the concentration of pentavalent dopants increases, the partial substitution of Sb^{5+} ions may be ionically compensated for by the formation of cation vacancies ($V_{Ti}^{''''}$). These vacancies, along with electrons, tend to accumulate in the negative space charge region [39]. This accumulation depletes $V_O^{\cdot\cdot}$ in the space charge region, slowing the diffusivity of O^{2-} between grains due to electric forces and the large ionic radius of O^{2-}. This reduction in grain mobility during sintering leads to limited grain growth in ZSTO ceramics at high doping concentrations compared with those at lower concentrations.

Figure 3 presents the SEM-EDX mapping analysis of the 5% ZSTO ceramics, which revealed a homogeneous dispersion of Zr, Sb, Ti, and O throughout the sample surface. This indicates the successful incorporation of Zr^{4+} and Sb^{5+} ions into the TiO_2 lattice. These findings are consistent with the XRD results, which confirm both the presence of the rutile phase and the effective substitution of Ti sites by Zr and Sb ions.

As shown in Fig. 4 and its inset, the giant ε' of the ZSTO ceramics remains highly consistent across varying measuring frequencies, whereas the low-frequency loss tangent (tanδ) values are relatively low. As detailed in Table 2, the giant ε' values are ~48,285, 72,323, and 73,964, whereas the corresponding low tanδ values are 0.106, 0.046, and 0.031 at 1 kHz and 25 °C for the 1%ZSTO, 2.5%ZSTO, and 5%ZSTO, respectively. These dielectric properties are comparable to those of other codoped TiO_2 ceramics [9,12,13,17,40]. Combining these findings with the SEM results, the increased ε' value with increasing dopant concentration inversely correlates with the mean grain size. The IBLC model alone cannot fully account for the dielectric behavior [41–44]. Broadband dielectric spectroscopy of co-doped TiO_2 ceramics reveals multiple sources of polarization that contribute to the overall dielectric response at ambient temperature [40].

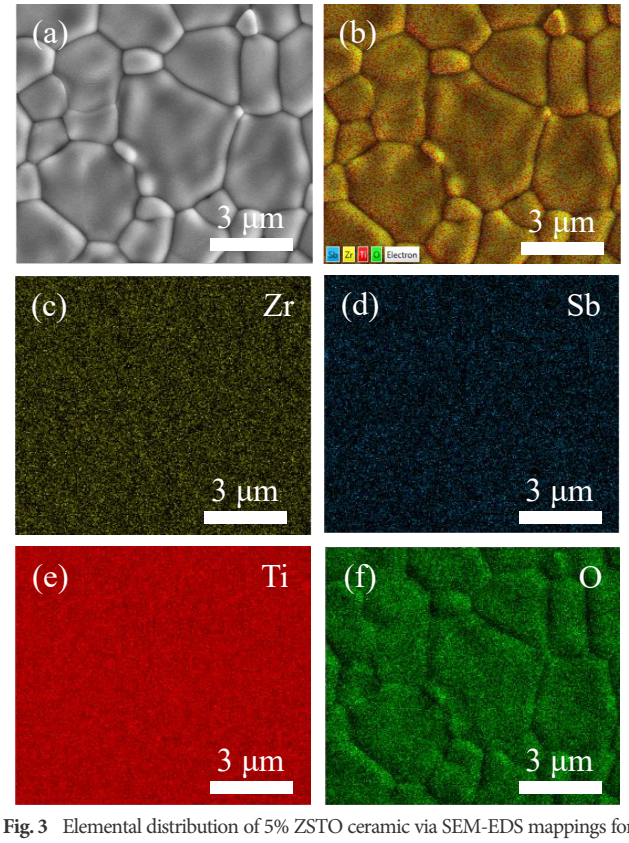

Fig. 3 Elemental distribution of 5% ZSTO ceramic via SEM-EDS mappings for (a) selected region, (b) all elements, (c) Zr, (d) Sb, (e) Ti, and (f) O.

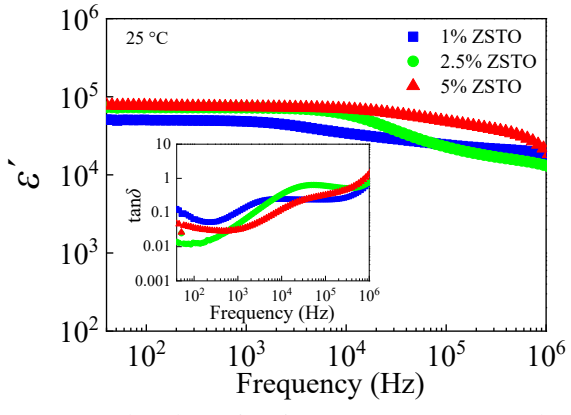

Fig. 4 Frequency dependence of ε' of ZSTO ceramics at 25 °C, with inset displaying tanδ frequency dependences.

Table 2 Humidity sensing properties of ZSTO ceramics and other capacitive ceramics at 25 °C: sensitivity at different frequencies, hysteresis error (γ_H), and response/recovery time (t_{Res} and t_{Rec})

Sample	Sensitivity (pF/%RH)@25 °C				Ref.
	@100 Hz	@480 Hz	@1 kHz	@10 kHz	
1%ZSTO*	210	93	66	34	This study
2.5%ZSTO*	672	437	345	140	This study
5%ZSTO*	400	283	237	122	This study
5%(Na/Nb) doped TiO_2**	102.6	—	—	—	[30]
10%(In/Nb) doped TiO_2**	229.2	—	—	—	[27]
Sample	Humidity sensing behavior@fixed frequency (f)@25 °C				Ref.
	γ_H (%)	f (Hz)	t_{Res} (s)	t_{Rec} (s)	
1%ZSTO*	2.0	10^3	61	45	This study
2.5%ZSTO*	1.6	10^3	30	20	This study
5%ZSTO*	1.6	10^3	12	16	This study
$CaCu_{2.6}Mg_{0.4}Ti_4O_{12}$***	7.0	10^3	858	1200	[8]
5%(Na/Nb) doped TiO_2**	4.2	10^2	115	20	[30]
10%(In/Nb) doped TiO_2**	7.33	10^2	165	30	[27]

Note: *Measured in the range of 30%–95% RH; **Measured in the range of 11%–96% RH; ***Measured in the range of 11%–97% RH.

Specifically, the effects of defect dipoles [41–44], hopping conduction [43], and interfacial polarization at the resistive outer surface layer and inner semiconducting core (SBLC) [43,44] or at the semiconductive surface/conductive electrode (S/E) interfaces likely play a significant role in the overall dielectric properties, as observed in other codoped TiO_2 ceramics [45–48].

To further understand the contribution of their dielectric properties, impedance spectroscopy (IS) analysis was conducted. The analysis revealed several significant findings: large semicircular arcs at low frequencies, as shown in Fig. 5(a); additional overlapping semicircular arcs at intermediate frequencies, as depicted in Fig. 5(b); and a nonzero intercept at high frequencies, as illustrated in the inset of Fig. 5(b). These results indicate the presence of at least three distinct electrical responses in ZSTO ceramics. The low resistivity observed at high frequencies, due to the non-zero intercept, could be attributed to the semiconductive grain response. Conversely, at intermediate and low frequencies, higher resistivity values may originate from insulative grain boundaries and interface effects near the surface, respectively. This electrically heterogeneous microstructure, comprising both insulating and semiconducting regions, plays a key role in the overall giant dielectric properties of the material. Typically, the low-frequency tanδ is closely related to the density of insulating grain boundary layers in polycrystalline ceramics [38]. The density of the grain boundary layers in the ZSTO ceramics increased as the co-doping concentration increased from 1% to 5% because of a reduction in the mean grain size. However, the low-frequency tanδ of the 5%ZSTO ceramics was greater than that of the 2.5%ZSTO ceramics, suggesting the formation of additional types of insulating layers in the ZSTO ceramics. These findings suggest interfacial polarization at various interfaces, as observed in (In/Nb), (Y/Nb), (Ho/Ta), and (Sn/Ta) codoped TiO_2 [19,47–49]. In the case of isovalent/pentavalent ion-doped TiO_2, such as (Zr^{4+}/Nb^{5+}) and (Zr^{4+}/Ta^{5+}) [17,50], defect clusters such as $Ti^{4+}\cdot e^- - V_O^{\cdot\cdot} - e^-\cdot Ti^{4+}$ could contribute to their dielectric performance. These defect clusters were also observed in $BaTiO_3$- and $SrTiO_3$-based materials [41–44], contributing to a giant dielectric response. These defect dipoles, considered lattice dipoles, form through the coupling of neighboring defects with opposite charges, leading to the creation of electron–pinned defect dipoles (EPDDs). Consequently, these effects could also influence the variation in the dielectric properties with humidity.

To study the humidity-sensing properties, C_p was measured at different frequencies and RH levels, ranging from 30% to 95% RH at 25 °C. The C_p values at 1 kHz for the ZSTO ceramics exhibited an almost linear dependence on the RH levels, with R^2 values of 0.903, 0.935, and 0.934 for 1%ZSTO, 2.5%ZSTO, and 5%ZSTO ceramics, respectively, in the 30%–95% RH range, as shown in Fig. 6(a). Notably, when the maximum RH was 85%, which falls within the normal operating range for commercial humidity sensors, the linearity values increased to 0.955, 0.970, and 0.951, respectively. This indicates that the nonlinearity ($1 - R^2$) for all samples is less than 0.1. As the RH increased from 30% to 95%, the C_p values at 1 kHz for the 2.5%ZSTO and 5%ZSTO ceramics increased by 152% and 114%, respectively, compared with a 50% increase for the 1%ZSTO ceramics. To assess their potential for gas sensing, we tested ZSTO ceramics with varying concentrations of hydrogen sulfide (H_2S) at 10 and 100 ppm. As shown in Fig. S2 in the ESM, the C_p values remained unchanged, even with increasing H_2S concentration, indicating that ZSTO ceramics are not suitable for H_2S gas sensing.

Figures 6(b) and 6(c) present the RH dependence of C_p at various frequencies for 2.5%ZSTO and 5%ZSTO ceramics, respectively. The trend of increasing C_p values with increasing RH is suppressed at higher frequencies for both samples, which is consistent with observations in other capacitive ceramics [5,8,27,30]. As the frequency increases, the applied electric field changes direction more rapidly than at lower frequencies,

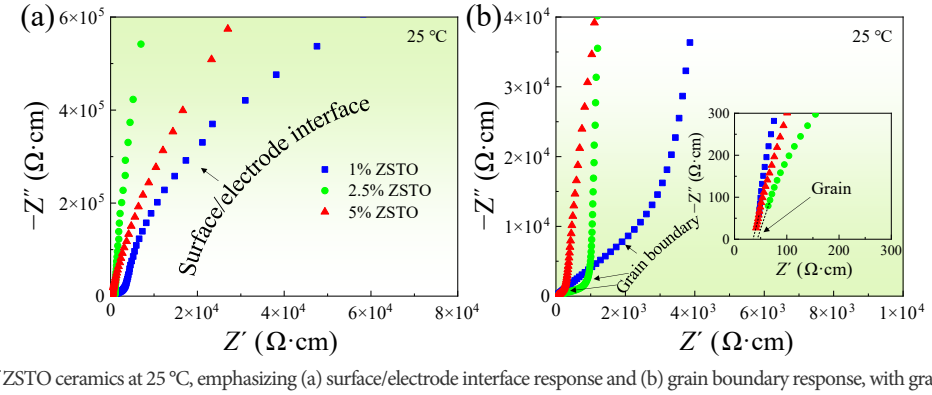

Fig. 5 IS plots of ZSTO ceramics at 25 °C, emphasizing (a) surface/electrode interface response and (b) grain boundary response, with grain response in inset.

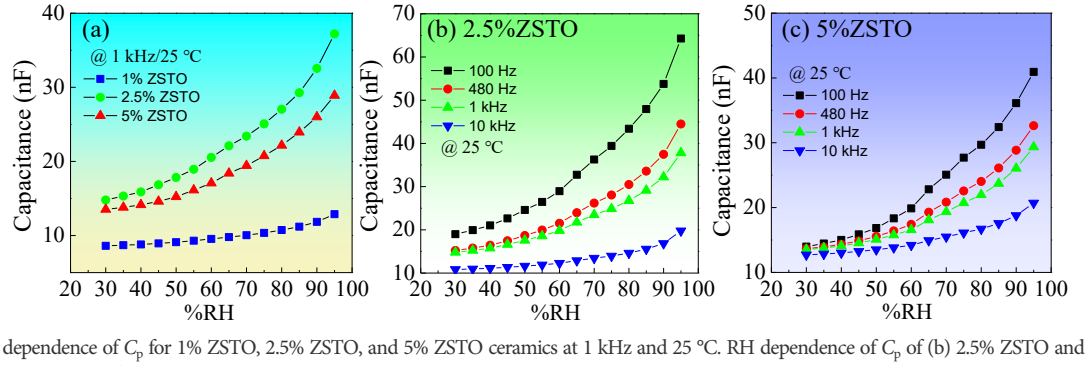

Fig. 6 (a) RH dependence of C_p for 1% ZSTO, 2.5% ZSTO, and 5% ZSTO ceramics at 1 kHz and 25 °C. RH dependence of C_p of (b) 2.5% ZSTO and (c) 5% ZSTO ceramics at 25 °C and various frequencies.

preventing the polarizations associated with adsorbed water molecules from fully aligning with the external field, resulting in lower C_p values. The sensitivity of the ceramics can be calculated via Eq. (1):

$$\text{Sensitivity} = \Delta C_p/\Delta\%\text{RH} \quad (1)$$

where ΔC_p is the change in C_p from the lowest to the highest %RH and where Δ%RH is the range of RH change. The sensitivity of the ZSTO ceramics, as listed in Table 2, decreases with increasing frequency, which is consistent with the results in Figs. 6(b) and 6(c). Notably, the sensitivity remains high even at frequencies up to 10 kHz—except for the sensitivity of the 1%ZSTO ceramics at frequencies higher than 480 Hz—which is comparable to the sensitivity at 100 Hz of other ceramics, such as NNTO and INTO [27,30]. This indicates that ZSTO ceramics are highly sensitive to humidity. Similar to the dielectric response, no clear correlation can be established between the sensitivity of ZSTO ceramics and their mean grain sizes at different co-doping concentrations.

Figure 7 depicts the humidity sensing behavior at 25 °C and 1 kHz of the 2.5%ZSTO and 5%ZSTO ceramics, with additional information on the 1%ZSTO ceramics provided in Fig. S3(a) in the ESM. In Figs. 7(a) and 7(b), the hysteresis behavior of both 2.5%ZSTO and 5%ZSTO ceramics is shown to be narrow. γ_H was calculated via Eq. (2) to assess the accuracy of the measurements during cycles of increasing RH (water absorption) and decreasing RH (water desorption).

$$\gamma_H = \pm\Delta H_{max}/2F_{FS} \quad (2)$$

where ΔH_{max} represents the maximum variation in C_p observed at identical RH levels during both the adsorption and desorption phases, and F_{FS} denotes the full scale of C_p differences observed across the entire RH range.

As listed in Table 2, the maximum γ_H values at 1 kHz for 1%ZSTO, 2.5%ZSTO, and 5%ZSTO ceramics are 2.0%, 1.6%, and 1.6%, respectively. These low γ_H values are smaller than those reported for other capacitive ceramics, such as $CaCu_{2.6}Mg_{0.4}Ti_4O_{12}$, $Na_{1/3}Ca_{1/3}Tb_{1/3}Cu_3Ti_4O_{12}$, $Na_{1/3}Sr_{1/3}Tb_{1/3}Cu_3Ti_4O_{12}$, ISTTO, CuO, NNTO, and INTO [8,22–24,27,28,30], indicating that ZSTO ceramics provide more reliable and accurate humidity sensing performance. A repeatability test was also performed. The ceramics were exposed to 30% RH for 5 min, followed by a rapid transition to 95% RH for 5 min to ensure full water absorption, and then quickly returned to 30% RH. This cycle was repeated to evaluate the consistency of their humidity-sensing response. Figures 7(c) and 7(d) show the repeatability results for the 2.5% ZSTO and 5% ZSTO ceramics, whereas Fig. S3(b) in the ESM presents the results for the 1% ZSTO ceramics. The results demonstrate that all the ZSTO ceramics exhibit reliable and consistent humidity-sensing performance at RH levels ranging from 30% to 95%.

The response and recovery time (t_{Res} and t_{Rec}) were determined. t_{Res} and t_{Rec} represent the time required for the C_p gain to reach 90% of the total C_p change during the transition from 30% to 95% RH and from 95% to 30% RH, respectively. As listed in Table 2 and illustrated in Figs. 7(e), 7(g), 7(f), and 7(h) and Fig. S3(c) in the ESM, the t_{Res}/t_{Rec} values are 61 s/45 s for 1%ZSTO ceramics, 30 s/20 s for 2.5%ZSTO ceramics, and 12 s/16 s for 5%ZSTO ceramics. These times indicate a faster response to humidity than other codoped TiO_2 ceramics do [27,28,30], as detailed in Table 2. Considering all humidity sensing characteristics, including sensitivity, γ_H, repeatability, and t_{Res}/t_{Rec} time, ZSTO ceramics exhibit outstanding humidity sensing properties compared with other capacitive humidity sensing materials [5,8,22–24,27,28,30], making them suitable for practical humidity sensors.

Figures 8(a) and 8(b) show the frequency dependences of ε' and tanδ (in the insets) for the 2.5%ZSTO and 5%ZSTO ceramics at various RH levels. Humidity significantly affects the ε' and tanδ spectra at frequencies below approximately 10^4 Hz. When the RH increased from 30% to 50%, a slight increase in low-frequency ε' was observed. This suggests that water molecules may interact with the exposed ceramic surface through chemisorption with defects, forming defect dipoles (discussed in more detail later) and contributing to the overall dielectric response and C_p. As RH further increased from 50% to 90%, a much greater increase in low-frequency ε' was observed, indicating that the large dielectric response at higher humidity levels cannot be attributed solely to additional defect dipoles. Notably, at 90% RH, ε' decreased almost linearly with increasing frequency from 40 to 10^4 Hz, suggesting that the dielectric response at these higher RH levels is strongly influenced by extrinsic effects, such as enhanced conduction. This is supported by the analysis in Figs. S4(a)–S4(d) in the ESM, where data fitting via the universal dielectric response equation $\varepsilon' \propto f^{s-1}$ (where f represents the frequency of the applied electric

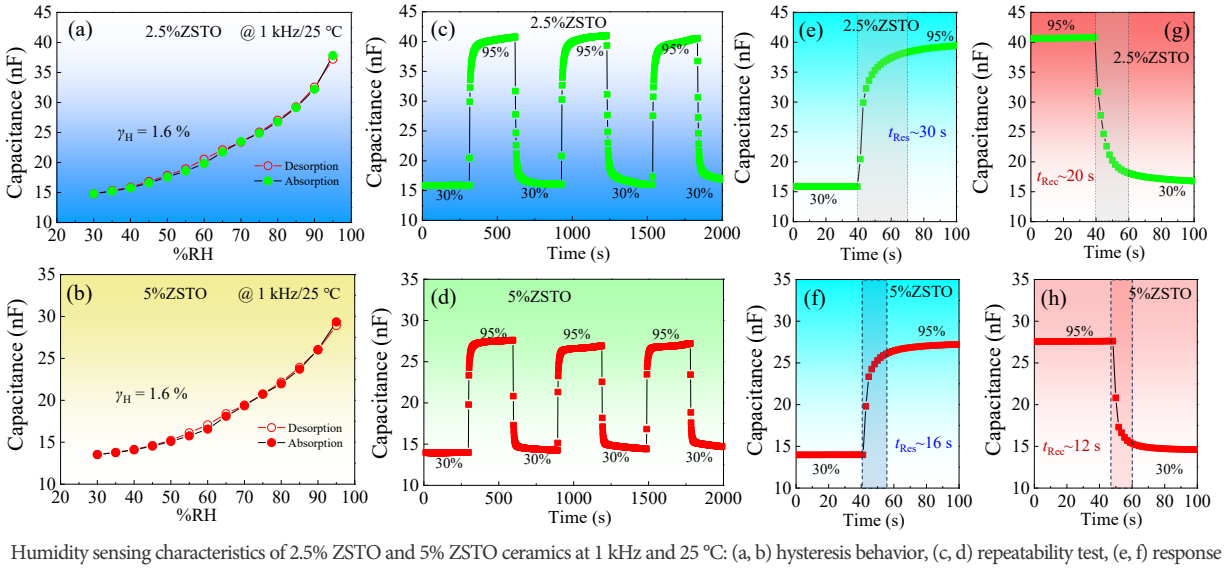

Fig. 7 Humidity sensing characteristics of 2.5% ZSTO and 5% ZSTO ceramics at 1 kHz and 25 °C: (a, b) hysteresis behavior, (c, d) repeatability test, (e, f) response time, and (g, h) recovery time.

field, and *s* denotes a constant value) [51], with $s = 0.66$, illustrates the contribution of conductivity at high RH levels. Additionally, extrinsic effects near the surface regions, such as the SBLC effect (and partially the IBLC effect), were further confirmed through the application of different direct current (DC) bias voltages, as shown in Figs. S5(a) and S5(b) in the ESM. The intrinsic and extrinsic mechanisms play critical roles in the humidity sensing behavior of ZSTO ceramics at low and high RH levels, respectively.

To gain insight into the ceramic surface properties, XPS spectra of the 5% ZSTO ceramics were analyzed to study the oxidation states of the elements present on the ceramic surface. Figure 9(a) shows the XPS spectra of Ti 2p with fitting curves. The peaks observed at 457.6, 458.5, 462.3, and 464.2 eV corresponded to Ti^{3+} $2p_{3/2}$, Ti^{4+} $2p_{3/2}$, Ti^{3+} $2p_{1/2}$, and Ti^{4+} $2p_{1/2}$, respectively. The splitting between Ti $2p_{1/2}$ and Ti $2p_{3/2}$ is 5.7 and 4.7 eV for Ti^{3+} and Ti^{4+}, respectively, which is consistent with observations in co-doped TiO_2 systems [14,17,34]. The detectable Ti^{3+} within the rutile structure could be due to the replacement of Ti^{4+} by Sb^{5+} ions, as expressed in Reactions (3) and (4) [52,53]:

$$2TiO_2 + Sb_2O_5 \xrightarrow{4TiO_2} 2Ti'_{Ti} + 2Sb^{\cdot}_{Ti} + 8O_o + 1/2O_2 \uparrow \quad (3)$$

$$Ti^{4+} + e' \rightarrow Ti^{3+} \quad (4)$$

Figure 9(b) shows the O 1s XPS spectra, which can be fitted by three peaks representing the oxygen lattice (529.7 eV) [9], oxygen lattices of other metal ions (i.e., Sb–O and Zr–O) (530.2 eV) [37], and hydroxyl groups (532.0 eV) [27,54]. The observed hydroxyl group likely results from water molecules adsorbed on the surface, confirming the ability of the material to absorb water from the ambient environment. This is further supported by the FTIR spectra shown in Fig. S6 in the ESM, where clear O–H stretching and bending modes were observed after 2.5%ZSTO ceramics were exposed to a 95% RH environment. These findings confirm the ability of ZSTO ceramics to interact with moisture, reinforcing their suitability for humidity sensing applications.

For ZSTO ceramics, doping Zr^{4+} ions into Ti^{4+} sites does not directly generate $V_O^{\cdot\cdot}$ directly, as supported by the XPS analysis. However, small amounts of $V_O^{\cdot\cdot}$ may still form due to the high sintering temperatures. In addition to free electrons introduced by Sb^{5+} doping (Reactions (3) and (4)), electrons can be further introduced into the ZSTO to compensate for the formation of $V_O^{\cdot\cdot}$, as explained by Reaction (5) [55,56]:

$$O_O^{\times} \rightarrow V_O^{\cdot\cdot} + 2e^- + 1/2O_2 \uparrow \quad (5)$$

To further investigate the presence of $V_O^{\cdot\cdot}$ caused by high-temperature sintering, Raman spectroscopy was employed. The E_g vibrational mode in the Raman spectrum is particularly sensitive to oxygen loss from the rutile-TiO_2 lattice, offering insights into potential $V_O^{\cdot\cdot}$ formation. The Raman spectra of ZSTO ceramics

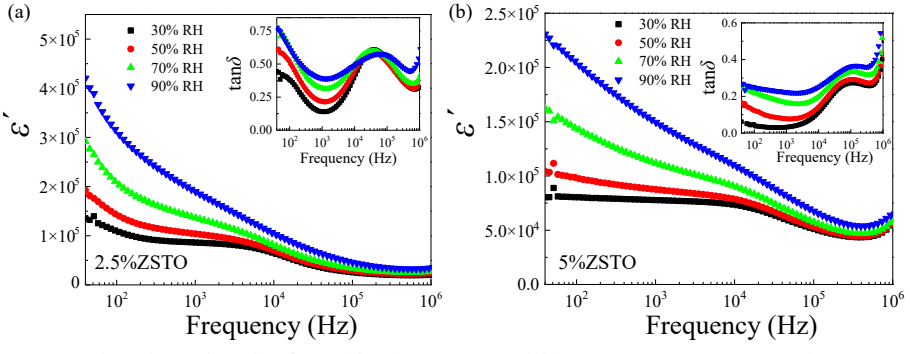

Fig. 8 Frequency dependence of ε' and tanδ (inset) for (a) 2.5% ZSTO and (b) 5% ZSTO ceramics at 25 °C and various RH levels.

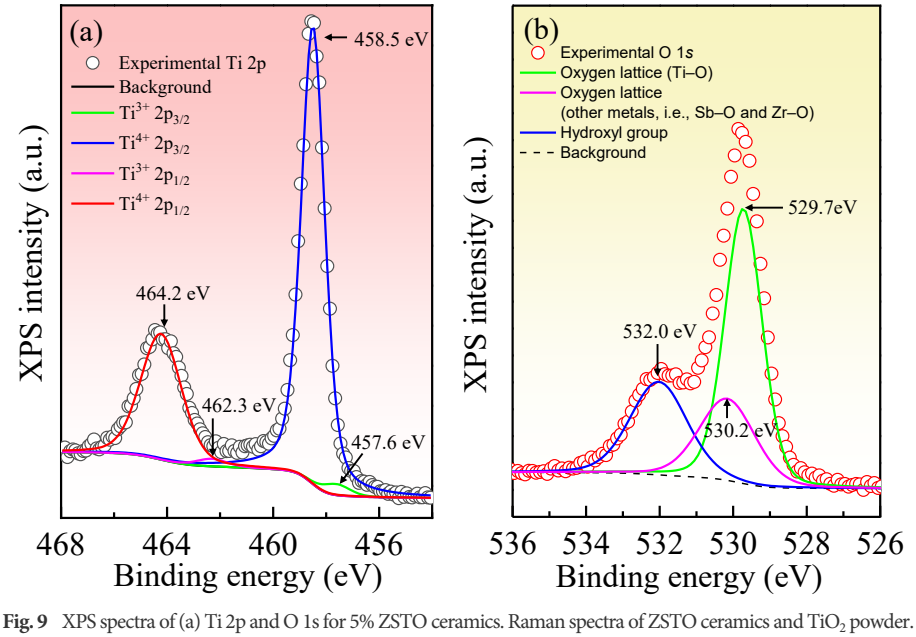

Fig. 9 XPS spectra of (a) Ti 2p and O 1s for 5% ZSTO ceramics. Raman spectra of ZSTO ceramics and TiO_2 powder.

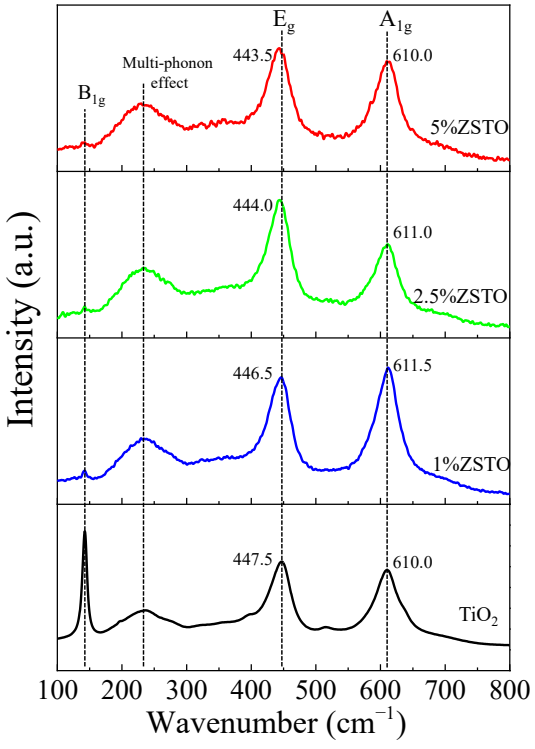

Fig. 10 Raman spectra of ZSTO ceramics and TiO_2 powder.

and TiO_2 powder are shown in Fig. 10, revealing four fundamental modes: B_{1g} mode, multi-phonon scattering, E_g mode, and A_{1g} mode. This indicates that the synthesized ZSTO ceramics contain the rutile phase, similar to TiO_2. Considering the E_g mode, which is related to oxygen atom liberation along the *c*-axis, the E_g peak of the TiO_2 powder (447.5 cm^{-1}), which is expected to have no $V_O^{\cdot\cdot}$, is comparable to the E_g peaks of the ZSTO ceramics. These peaks tend to shift to lower wavenumbers as the dopant concentration increases (446.5 cm^{-1} → 444.0 cm^{-1} → 443.5 cm^{-1} for 1%ZSTO, 2.5%ZSTO, and 5%ZSTO, respectively). This shift could be due to an increase in the formation of $V_O^{\cdot\cdot}$ caused by the sintering process at high temperatures, as previously discussed. Moreover, the A_{1g} peak, related to a vibrational mode that corresponds to the symmetric stretching of the Ti–O bonds in the TiO_2 lattice, did not significantly change with the dopant concentration (610.0 cm^{-1} for TiO_2 powder, 611.5, 611.0, and 610.0 cm^{-1} for 1%ZSTO, 2.5%ZSTO, and 5%ZSTO, respectively). The ionic radius of Sb^{5+} is not significantly different from that of Ti^{4+}, whereas Zr^{4+} is an isovalent dopant. Therefore, both ions may only slightly affect the Ti–O stretching modes.

The XPS and Raman results confirmed the formation of EPDDs from defect clusters ($Ti^{4+}\cdot e^- - V_O^{\cdot\cdot} - e^-\cdot Ti^{4+}$), which contributed to the overall dielectric response at room temperature [41,42]. Additionally, the existence of point defects, such as $Sb_{Ti}^{\cdot}$ and $V_O^{\cdot\cdot}$, as presented in Reactions (3) and (5) could play a crucial role in interacting with water molecules, thereby serving as active centers for humidity sensors in ZSTO ceramics, as reported in NNTO, (In/Nb) codoped SnO_2, and (In/Nb) codoped HfO_2 ceramics [6,7,30]. In the case of the $V_O^{\cdot\cdot}$ active center, water molecules (H_2O) can be captured by $V_O^{\cdot\cdot}$ and react with oxygen atoms (O_O) in the materials to form hydroxyl radicals, as expressed in Reaction (6):

$$H_2O + V_O^{\cdot\cdot} + O_O \rightarrow 2OH_O^{\cdot} \quad (6)$$

Moreover, the $Sb_{Ti}^{\cdot}$ active center can split water molecules into hydrogen ions (H^+) and hydroxide ions (OH^-) via an electrostatic field, as displayed in Reaction (7):

$$2H_2O \rightarrow 2H^+ + 2OH^- \quad (7)$$

Water molecules dissociate into H^+ and OH^- under local electrostatic fields, forming $H^+ - OH^-$ dipoles. This adsorption process, involving $Sb_{Ti}^{\cdot}$ and $V_O^{\cdot\cdot}$ as active centers, is termed chemisorption and represents the initial stage of water interaction with the ceramic surface. The generated OH^- and H^+ ions can associate with point defects such as $Ti_{Ti}^{'}$ ($Ti^{4+} + e^-$), $V_O^{\cdot\cdot}$, and $Sb_{Ti}^{\cdot}$, forming complex defect dipoles such as $Ti^{4+}\cdot e^- - H^+$, $Ti^{4+}\cdot e^- - OH_O^{\cdot}$, $Sb_{Ti}^{\cdot} - OH^-$, and $OH^- - V_O^{\cdot\cdot} - OH^-$. These dipoles can reorient in response to an applied electric field, increasing the C_p value through dipolar polarization. At low RH levels, the concentration of water molecules and, consequently, H^+ and OH^- ions remain low, leading to poor surface conduction and negligible interfacial polarization effects, as illustrated in Figs. 6–8. This is evidenced by a slight increase in C_p at higher frequency ranges, as shown in Figs. 6(b) and 6(c), where interfacial polarization typically dominates at lower frequencies.

As the RH increases, more water molecules begin to form a continuous water layer, known as physisorption, which enhances the conduction of protons as follows: $H_3O^+ \rightarrow H^+ + H_2O$. With further increases in the RH, multiple water layers can form, leading to the transfer of H_2O and H_3O^+ ions, as described by the Grotthuss chain reaction [57]: $H_2O + H_3O^+ \rightarrow H_3O^+ + H_2O$. These phenomena correspond to the IS plots of the ZSTO ceramics at different RH levels, as presented in Fig. S7 in the ESM. The semicircular arcs due to the S/E (or surface layer effect) and grain boundary responses noticeably decrease with increasing RH, indicating a decrease in resistivity due to the S/E and grain boundary effects, as shown in Figs. S7(a), S7(c), and S7(e) in the ESM and Figs. S7(b), S7(d), and S7(f) in the ESM, respectively. Moreover, the resistivity due to grains of the ZSTO ceramics does not change with increasing RH, as presented in the insets of Figs. S7(b), S7(d), and S7(f) in the ESM, where their non-zero intercepts appear to remain unchanged despite variations in humidity. The increased C_p values with increasing RH in the ZSTO ceramics could be attributed to changes in the electrical properties of the ceramic surface and grain boundaries at the outermost layer. The possible formation of a dipole of $H^+ - OH^-$ and the jumping of H^+ and H_3O^+ ions on the ceramic surface could lead to an increase in the dielectric polarization mechanism, resulting in varied C_p values. Additionally, the H^+ and OH^- groups also localize along the grain boundaries, promoting interfacial polarization, which increases the C_p values. Accordingly, the origin of capacitive humidity sensing mechanisms in ZSTO could arise from changes in the capacitive/impedance properties of the ceramic surface and grain boundaries.

To further clarify the humidity-sensing mechanisms at high RH levels, the roles of the surface layer and grain boundary response were investigated. As shown in Fig. S8(a) in the ESM, two different electrode configurations were employed. Configuration-I, which had a larger exposed surface area, demonstrated significantly higher $\Delta C_p/C_{p\,(30\%RH)}$ values than did Configuration-II, where both surfaces were fully coated with Ag electrodes (Figs. S8(b)–S8(d) in the ESM). This indicated the critical role of the exposed surface in humidity sensitivity. The increased C_p values in Configuration-I can be attributed to extrinsic surface effects, including the SBLC and S/E effects, as well as the increased grain boundary response due to water molecule absorption along the grain boundaries. However, even with full surface coverage, the samples still exhibited notable C_p changes at high RH levels, indicating that, beyond surface effects, the grain boundaries near

the edges of the ceramics remained responsive to humidity. These results suggest that both surface interactions and grain boundary effects play key roles in the humidity sensing mechanisms of ZSTO ceramics.

4 Conclusions

ZSTO ceramics with high-density microstructures were successfully prepared via the SSR method and exhibited significantly large ε' values ranging from ~4.82×10^4 to 7.39×10^4, along with low tanδ values (~0.031–0.106) at 25 °C and 1 kHz. Remarkable humidity-sensing properties were observed in the ZSTO ceramics. Among the samples studied, the 5% ZSTO ceramics exhibited optimal humidity sensing characteristics at 1 kHz, with a high sensitivity of 283 pF/%RH, a low γ_H of ~1.6%, and fast response/recovery time of 12 and 16 s, respectively. $Sb_{Ti}^{\cdot}$ and $V_O^{\cdot\cdot}$, as evidenced by the XPS results, were identified as the active centers for water detection. According to IS studies, the humidity-sensing mechanism in ZSTO ceramics could be attributed to changes in the electric/dielectric properties of the ceramic surface and grain boundaries, which also involve the conduction of H^+ and H_3O^+ through the Grotthuss chain reaction.

Acknowledgements

This project is funded by the National Research Council of Thailand (NRCT) (No. N41A640084). This project was also funded by the National Science, Research, and Innovation Fund (NSRF) and the Fundamental Fund, and Graduate Studies Office of Khon Kaen University. This work has received a scholarship under the Post Doctoral Training for Frontier Research from Khon Kaen University, Thailand (No. PD2567-07).

Declaration of competing interest

The authors have no competing interests to declare that are relevant to the content of this article.

Electronic Supplementary Material

Supplementary material is available in the online version of this article at https://doi.org/10.26599/JAC.2024.9221005.

References

[1] Chen Z, Lu C. Humidity sensors: A review of materials and mechanisms. *Sens Lett* 2005, **3**: 274–295.
[2] Lee CY, Lee GB. Humidity sensors: A review. *Sens Lett* 2005, **3**: 1–15.
[3] Traversa E. Ceramic sensors for humidity detection: The state-of-the-art and future developments. *Sensor Actuat B Chem* 1995, **23**: 135–156.
[4] Krishna Prasad NV, Venkata Prasad K, Ramesh S, *et al.* Ceramic sensors: A mini-review of their applications. *Front Mater* 2020, **7**: 593342.
[5] Li M. Study of the humidity-sensing mechanism of $CaCu_3Ti_4O_{12}$. *Sensor Actuat B Chem* 2016, **228**: 443–447.
[6] Yao JH, Wang JS, Cao WJ, *et al.* Humidity sensing properties of (In + Nb) doped HfO_2 ceramics. *Nanomaterials-Basel* 2023, **13**: 951.
[7] Wang J, Guo YM, Wang ST, *et al.* The effect of humidity on the dielectric properties of (In + Nb) co-doped SnO_2 ceramics. *J Eur Ceram Soc* 2019, **39**: 323–329.
[8] Li M, Chen XL, Zhang DF, *et al.* Humidity sensitive properties of pure and Mg-doped $CaCu_3Ti_4O_{12}$. *Sensor Actuat B Chem* 2010, **147**: 447–452.
[9] Hu WB, Liu Y, Withers RL, *et al.* Electron-pinned defect-dipoles for high-performance colossal permittivity materials. *Nat Mater* 2013, **12**: 821–826.
[10] Peng H, Liang PF, Zhou XB, *et al.* Good thermal stability, giant permittivity, and low dielectric loss for X9R-type $(Ag_{1/4}Nb_{3/4})_{0.005}Ti_{0.995}O_2$ ceramics. *J Am Ceram Soc* 2019, **102**: 970–975.
[11] Peng H, Liang PF, Wu D, *et al.* Simultaneous realization of broad temperature stability range and outstanding dielectric performance in (Ag^+, Ta^{5+}) co-doped TiO_2 ceramics. *J Alloys Compd* 2019, **783**: 423–427.
[12] Yang C, Tse MY, Wei XH, *et al.* Colossal permittivity of (Mg + Nb) co-doped TiO_2 ceramics with low dielectric loss. *J Mater Chem C* 2017, **5**: 5170–5175.
[13] Dong W, Chen DH, Hu WB, *et al.* Colossal permittivity behavior and its origin in rutile $(Mg_{1/3}Ta_{2/3})_xTi_{1-x}O_2$. *Sci Rep* 2017, **7**: 9950.
[14] Liu GC, Fan HQ, Xu J, *et al.* Colossal permittivity and impedance analysis of niobium and aluminum co-doped TiO_2 ceramics. *RSC Adv* 2016, **6**: 48708–48714.
[15] Mingmuang Y, Chanlek N, Moontragoon P, *et al.* Effects of Sn^{4+} and Ta^{5+} dopant concentration on dielectric and electrical properties of TiO_2: Internal barrier layer capacitor effect. *Results Phys* 2022, **42**: 106029.
[16] Peng P, Chen CH, Cui B, *et al.* Influence of the electric field on flash-sintered (Zr + Ta) co-doped TiO_2 colossal permittivity ceramics. *Ceram Int* 2022, **48**: 6016–6023.
[17] Yang C, Wei XH, Hao JH. Colossal permittivity in TiO_2 co-doped by donor Nb and isovalent Zr. *J Am Ceram Soc* 2018, **101**: 307–315.
[18] Li JL, Li F, Li C, *et al.* Evidences of grain boundary capacitance effect on the colossal dielectric permittivity in (Nb + In) co-doped TiO_2 ceramics. *Sci Rep* 2015, **5**: 8295.
[19] Nachaithong T, Kidkhunthod P, Thongbai P, *et al.* Surface barrier layer effect in (In + Nb) co-doped TiO_2 ceramics: An alternative route to design low dielectric loss. *J Am Ceram Soc* 2017, **100**: 1452–1459.
[20] Crandles DA, Yee SMM, Savinov M, *et al.* Electrode effects in dielectric spectroscopy measurements on (Nb + In) co-doped TiO_2. *J Appl Phys* 2016, **119**: 154105.
[21] Siriya P, Tuichai W, Danwittayakul S, *et al.* Surface layer characterizations and sintering time effect on electrical and giant dielectric properties of $(In_{0.05}Nb_{0.05})Ti_{0.9}O_2$ ceramics. *Ceram Int* 2018, **44**: 7234–7239.
[22] Srilarueang S, Putasaeng B, Sreejivungsa K, *et al.* Giant dielectric response, nonlinear characteristics, and humidity sensing properties of a novel perovskite: $Na_{1/3}Sr_{1/3}Tb_{1/3}Cu_3Ti_4O_{12}$. *RSC Adv* 2023, **13**: 29706–29720.
[23] Srilarueang S, Sreejivungsa K, Thanamoon N, *et al.* Optimizing sintering conditions and microstructure for enhanced dielectric and humidity sensing properties of $Na_{1/3}Ca_{1/3}Tb_{1/3}Cu_3Ti_4O_{12}$ ceramics. *Mater Chem Phys* 2024, **318**: 129320.
[24] Sreejivungsa K, Thanamoon N, Phromviyo N, *et al.* Advanced humidity sensing properties of CuO ceramics. *Sci Rep* 2024, **14**: 9726.
[25] Liu LJ, Fan HQ, Fang L, *et al.* Dielectric characteristic of nanocrystalline $Na_{0.5}K_{0.5}NbO_3$ ceramic green body. *J Electroceram* 2012, **28**: 144–148.
[26] Liu LJ, Wu MX, Yang Z, *et al.* Dielectric relaxation of NKN–BNT porous green body. *Procedia Engineer* 2012, **27**: 793–798.
[27] Si RJ, Li TY, Sun J, *et al.* Humidity sensing behavior and its influence on the dielectric properties of (In + Nb) co-doped TiO_2 ceramics. *J Mater Sci* 2019, **54**: 14645–14653.
[28] Wongsricha J, Sreejivungsa K, Thanamoon N, *et al.* Enhanced humidity sensing properties of Ta_2O_5 and ITO doped rutile-TiO_2 porous ceramics. *Sci Rep* 2024, **14**: 18656.
[29] Li TY, Si RJ, Sun J, *et al.* Giant and controllable humidity sensitivity achieved in (Na + Nb) codoped rutile TiO_2. *Sensor Actuat B-Chem* 2019, **293**: 151–158.
[30] Li TY, Si RJ, Wang J, *et al.* Microstructure, colossal permittivity, and humidity sensitivity of (Na,Nb) co-doped rutile TiO_2 ceramics. *J Am Ceram Soc* 2019, **102**: 6688–6696.
[31] Mingmuang Y, Chanlek N, Moontragoon P, *et al.* Significantly improved dielectric properties of tin and niobium co-doped rutile

TiO_2 driven by Maxwell–Wagner polarization. *J Alloys Compd* 2022, **923**: 166371.
[32] Wongsricha J, Sreejivungsa K, Thanamoon N, *et al.* Low loss tangent and excellent humidity–temperature stability with DC bias independence of giant-permittivity TiO_2 doped with indium tin oxide and tantalum pentoxide. *Ceram Int* 2024, **50**: 1547–1555.
[33] Boonlakhorn J, Putasaeng B, Kidkhunthod P, *et al.* First-principles calculations and experimental study of enhanced nonlinear and dielectric properties of Sn^{4+}-doped $CaCu_{2.95}Mg_{0.05}Ti_4O_{12}$ ceramics. *J Eur Ceram Soc* 2021, **41**: 5176–5183.
[34] Han H, Dufour P, Mhin S, *et al.* Quasi-intrinsic colossal permittivity in Nb and in co-doped rutile TiO_2 nanoceramics synthesized through a oxalate chemical-solution route combined with spark plasma sintering. *Phys Chem Chem Phys* 2015, **17**: 16864–16875.
[35] Shannon RD. Revised effective ionic radii and systematic studies of interatomic distances in halides and chalcogenides. *Acta Cryst A* 1976, **A32**: 751–767.
[36] Rahaman MN. *Ceramic Processing and Sintering.* Boca Raton (USA): CRC Press, 2003.
[37] Tuichai W, Thongyong N, Danwittayakul S, *et al.* Very low dielectric loss and giant dielectric response with excellent temperature stability of Ga^{3+} and Ta^{5+} co-doped rutile-TiO_2 ceramics. *Mater Design* 2017, **123**: 15–23.
[38] Boonlakhorn J, Chanlek N, Manyam J, *et al.* Enhanced giant dielectric properties and improved nonlinear electrical response in acceptor–donor (Al^{3+},Ta^{5+})-substituted $CaCu_3Ti_4O_{12}$ ceramics. *J Adv Ceram* 2021, **10**: 1243–1255.
[39] Chiang YM, Takagi T. Grain-boundary chemistry of barium titanate and strontium titanate: I, high-temperature equilibrium space charge. *J Am Ceram Soc* 1990, **73**: 3278–3285.
[40] Thongyong N, Chanlek N, Srepusharawoot P, *et al.* Experimental study and DFT calculations of improved giant dielectric properties of Ni^{2+}/Ta^{5+} co-doped TiO_2 by engineering defects and internal interfaces. *J Eur Ceram Soc* 2022, **42**: 4944–4952.
[41] Li CL, Huang C, Zhu ML, *et al.* Defect engineering in rare-earth-doped $SrTiO_3$ ceramics: Route to colossal capacitance material up to X9R capacitor standard. *Mater Today Commun* 2024, **39**: 108680.
[42] Li CL, Huang C, Zhu ML, *et al.* High-resistance X9R-type colossal dielectric ceramics achieved by reducing grain size in Y-modified $SrTiO_3$. *J Am Ceram Soc* 2024, **107**: 4223–4231.
[43] Huang C, Meng YZ, Li CL, *et al.* Colossal permittivity, low dielectric loss, and good thermal stability achieved in Ta-doped $BaTiO_3$ by B-site defect engineering. *J Mater Sci Mater El* 2023, **34**: 2231.
[44] Meng YZ, Liu K, Zhang XY, *et al.* Defect engineering in rare-earth-doped $BaTiO_3$ ceramics: Route to high-temperature stability of colossal permittivity. *J Am Ceram Soc* 2022, **105**: 5725–5737.
[45] Nachaithong T, Thongbai P, Maensiri S. Colossal permittivity in $(In_{1/2}Nb_{1/2})_xTi_{1-x}O_2$ ceramics prepared by a glycine nitrate process. *J Eur Ceram Soc* 2017, **37**: 655–660.
[46] Tuichai W, Danwittayakul S, Chanlek N, *et al.* Origin(s) of the apparent colossal permittivity in $(In_{1/2}Nb_{1/2})_xTi_{1-x}O_2$: Clarification on the strongly induced Maxwell–Wagner polarization relaxation by DC bias. *RSC Adv* 2017, **7**: 95–105.
[47] Wang XW, Zhang BH, Xu LH, *et al.* Dielectric properties of Y and Nb co-doped TiO_2 ceramics. *Sci Rep* 2017, **7**: 8517.
[48] Mingmuang Y, Chanlek N, Srepusharawoot P, *et al.* Origin of excellent giant dielectric performance of rutile-TiO_2 ceramics codoped with isovalent/pentavalent dopants. *Mater Res Bull* 2022, **155**: 111964.
[49] Fan JT, Long Z, Zhou HT, *et al.* Colossal dielectric behavior of (Ho, Ta) co-doped rutile TiO_2 ceramics. *J Mater Sci Mater El* 2021, **32**: 14780–14790.
[50] Mingmuang Y, Chanlek N, Thongbai P. Ultra–low loss tangent and giant dielectric permittivity with excellent temperature stability of TiO_2 co-doped with isovalent-Zr^{4+}/pentavalent-Ta^{5+} ions. *J Materiomics* 2022, **8**: 1269–1277.
[51] Lunkenheimer P, Krohns S, Riegg S, *et al.* Colossal dielectric constants in transition-metal oxides. *Eur Phys J Spec Top* 2009, **180**: 61–89.
[52] Fan JT, Leng SL, Cao ZZ, *et al.* Colossal permittivity of Sb and Ga co-doped rutile TiO_2 ceramics. *Ceram Int* 2019, **45**: 1001–1010.
[53] Li ZW, Wu JG. Novel titanium dioxide ceramics containing bismuth and antimony. *J Materiomics* 2017, **3**: 112–120.
[54] Si RJ, Xie XJ, Li TY, *et al.* TiO_2/$NaNbO_3$ heterojunction for boosted humidity sensing ability. *Sensor Actuat B Chem* 2020, **309**: 127803.
[55] Tuichai W, Danwittayakul S, Chanlek N, *et al.* High-performance giant-dielectric properties of rutile TiO_2 co-doped with acceptor-Sc^{3+} and donor-Nb^{5+} ions. *J Alloys Compd* 2017, **703**: 139–147.
[56] Zhao XG, Liu P. Effects of sintering atmosphere on microstructure and dielectric properties of (Yb + Nb) co-doped rutile TiO_2 ceramics. *J Alloys Compd* 2017, **715**: 170–175.
[57] Agmon N. The Grotthuss mechanism. *Chem Phys Lett* 1995, **244**: 456–462.